Structural Analysis and Electrochemical Properties of Bimetallic Palladium–Platinum Aerogels Prepared by a Two-Step Gelation Process

Mehtap Oezaslan,*[a, b] Anne-Kristin Herrmann,[c] Matthias Werheid,[c] Anatoly I. Frenkel,[d] Maarten Nachtegaal,[a] Carsten Dosche,[b] Céline Laugier Bonnaud,[a, e] Hale Ceren Yilmaz,[a, f] Laura Kühn,[c] Erhard Rhiel,[g] Nikolai Gaponik,[c] Alexander Eychmüller,[c] and Thomas Justus Schmidt*[a, h]

Multimetallic aerogels have emerged as promising unsupported and high-surface-area metal materials for different applications in heterogeneous catalysis and electrochemistry, which are fabricated using a gelation process characterized by the controlled aggregation of metallic nanoparticles to form a macroscopic network structure in aqueous solution. However, the achievement of the structural homogeneity of the multimetallic aerogels in terms of the diameter of the nanochains and the chemical composition at the nano- and the macro-scale is still a great challenge. In this paper, we investigated two Pd-Pt aerogels prepared by the two-step gelation method. The structural homogeneity and chemical distribution of both metals inside the aerogels were analyzed by using high-resolution (scanning) transmission microscopy, energy-dispersive X-ray spectroscopy, extended X-ray absorption fine structure spectroscopy and cyclic voltammetry. The Pd-Pt aerogels show the presence of Pd/Pt-rich domains inside the long-range framework. It is evident that the initial monometallic features dominate over alloying during the gelation process. Although the same synthetic approach for Pd-Pt aerogels with different atomic ratios was used, we observed that the sizes of these monometallic domains varied strongly between the Pd-rich and Pt-rich aerogels. The presence of such metal clusters influenced the electrochemical robustness of the Pd-Pt aerogels dramatically. Electrochemical durability investigations revealed that the aerogels with a high content of Pd are less stable because of the gradual dissolution of the less noble metal particularly inside the Pd-rich domains. A chemical and structural homogeneity might improve the lifetime of the Pd-Pt aerogels under electrochemical conditions. In this work, we provide a better understanding of the structure and chemical distribution of the bimetallic aerogel framework prepared by the two-step gelation process.

Introduction

Recently, multimetallic aerogels have attracted great attention in heterogeneous catalysis and electrochemical reactions.[1] Unsupported metallic materials such as aerogels, nanowires, nanotubes, nanoplates, and nanostructured films are of large

[a] Prof. Dr. M. Oezaslan, Dr. M. Nachtegaal, C. Laugier Bonnaud, H. C. Yilmaz, Prof.Dr. T. J. Schmidt
Paul Scherrer Institut
CH-5232 Villigen PSI (Switzerland)
E-mail: thomasjustus.schmidt@psi.ch

[b] Prof. Dr. M. Oezaslan, Dr. C. Dosche
Physical Chemistry
Carl von Ossietzky University of Oldenburg
26111 Oldenburg (Germany)
E-mail: mehtap.oezaslan@uni-oldenburg.de

[c] Dr. A.-K. Herrmann, M. Werheid, L. Kühn, Prof.Dr. N. Gaponik, Prof. Dr. A. Eychmüller
Physical Chemistry
TU Dresden
01062 Dresden (Germany)

[d] Prof.Dr. A. I. Frenkel
Department of Materials Science and Chemical Engineering
Stony Brook University
Stony Brook, NY 11794 (USA)

[e] C. Laugier Bonnaud
Present address:
AlpesLaboratoire O'Electrochimie et de Physico-chimie des Matériaux et des Interfaces
University of Grenoble 38000 Grenoble (France)

[f] H. C. Yilmaz
Present address:
Laboratory of Inorganic Chemistry
ETH Zurich
8093 Zurich (Switzerland)

[g] Dr. E. Rhiel
Light and Electron Microscopy Service Unit of the
School of Mathematics and Science
Carl von Ossietzky University of Oldenburg
26111 Oldenburg (Germany)

[h] Prof.Dr. T. J. Schmidt
Laboratory of Physical Chemistry
ETH Zurich
8093 Zurich (Switzerland)

🖳 Supporting information for this article can be found under:
http://dx.doi.org/10.1002/cctc.201600667

interest because of their high conductivity, high resistance, and catalytic performance for (electro)chemical reactions.[2] Metal aerogels are a new class of unsupported materials with a low density, high porosity, and large surface area. The 3D metal framework structure is formed by nanoparticles that are well connected and linked with each other. As a result of their unique structure, aerogels have the potential to combine the physical and chemical properties of nanomaterials and macroscopic materials. The chemical, physical, and (electro)catalytic properties of multimetallic aerogels can be tuned by varying the chemical composition, size, and shape of the nanoparticles that act as building units and the linking to gain a large surface area and high porosity.[1a, d, k, 3]

In the last few years, a broad range of synthetic methods has been developed to design multimetallic aerogels with various chemical compositions, structures, and morphologies.[1b–f, h, 4] In particular, two main synthetic approaches for the preparation of multimetallic aerogels have been developed: (i) a spontaneous one-step gelation process[1b–d] and (ii) a two-step gelation process.[1d, e] The gelation process is, generally, described as the connection and linking of nanoparticles to form a long-range-ordered 3D hydrogel in aqueous solution as the primary stage for the preparation of aerogels. During the one-step gelation process, the formation of hydrogel takes place spontaneously. In contrast, in the two-step gelation process, first a stable colloidal sol that contains monodisperse nanoparticles is synthesized by the chemical reduction of metal precursor salts, and then the formation of the hydrogel is induced by the destabilization of the colloidal suspension. The drying process or, more precisely, the exchange of the solvent for the transformation of hydrogels into aerogel monoliths is similar in both synthetic approaches. A mild drying process, such as supercritical CO_2 drying, can be applied to avoid the shrinkage and collapse of the metal framework. Altogether, the gelation process is the crucial step for the preparation of multimetallic aerogels and influences their final morphology and chemical composition strongly and thus their resulting mechanical, chemical, and (electro)catalytic properties.

The electrocatalytic properties of multimetallic materials differ significantly from those of the monometallic counterparts. The alteration of the activities is based largely on electronic effects,[5] ensemble effects,[6] and geometric effects[5b,7] (based on the mismatch of lattice parameters). These effects rarely appear alone, and it is often difficult to distinguish between them. In most cases, it is even desired that synergetic effects between electronic and geometric effects based on the mixture of dissimilar atoms are present to further improve the reactivity, selectivity, and durability of these multimetallic materials. Recently, unsupported Pd-Pt aerogels prepared by the one-step gelation process have emerged as a promising electrocatalyst for the oxygen reduction reaction (ORR; $O_2 + 4H^+ + 4e^- \rightarrow 2H_2O$, $E^0 = 1.23$ V), which takes place at the cathode side of fuel cells.[1b,d] Improvements of the catalytic activity and durability and reduced costs for this reaction may help to spread the worldwide application of fuel cell systems. Here, we present a distinctly different synthetic route for bimetallic aerogels than that published previously. The bimetallic aerogels presented in this work were prepared by a two-step gelation process. The BET surface areas of this class of unsupported metallic aerogels are in the range of 60–80 $m^2 g^{-1}$, and compared to other unsupported metallic materials, the aerogels clearly show larger surface areas.[1d, e]

The relationships between reactivity and lifetime are correlated strongly with the structure and the chemical composition of these aerogels. High structural homogeneity and a defined chemical composition are needed, yet this can be a great challenge for macroscopic aerogels that form during the gelation process at ambient or low temperatures of 70–90 °C. This challenge, generally, is faced by all self-assembled nanostructured multimetallic materials such as nanowires, nanotubes, and nanoporous materials. Therefore, a broad range of high-resolution microscopic and spectroscopic techniques is required to characterize these nanostructured materials on different length scales (which range from the Ångstrom-scale to the macroscale). The combination of several techniques is essential to provide information about the structure and chemical composition of these unsupported multimetallic materials over a broad length scale. In particular, it is difficult to analyze the Pd-Pt aerogel system by using XRD because of the similar lattice parameters and small crystallite sizes. A well-known strategy to improve the chemical homogeneity in nanostructured multimetallic materials is thermal treatment at high temperatures.[8] However, in most cases, a typical side-effect is the loss of the nanostructure by agglomeration and the collapse of the fragile network structure which result in a drastic decrease of the surface area.

In this work, we investigated the homogeneity and chemical distribution of the self-assembled Pd-Pt aerogels prepared by the two-step gelation process. Pure Pd, pure Pt, and Pd-Pt systems show a face-centered cubic (fcc) crystal structure with a space group of $Fm\bar{3}m$. As the lattice parameters of pure Pt and Pd metals are very similar (3.8870 Å for Pd and 3.9250 Å for Pt obtained from the Inorganic Crystal Structure Database (ICSD)[9]) and because of the presence of nano-sized domains, crystal-phase identification by using Rietveld refinement is not meaningful for these materials. Based on the combined results from high-resolution (scanning) transmission microscopy energy-dispersive X-ray spectroscopy (HR(S)TEM-EDX) and extended X-ray absorption fine structure (EXAFS) spectroscopy, the distributions of the Pd and Pt atoms inside the aerogel framework prepared by the two-step gelation process were revealed. We observed that the initial structure of the monometallic domains resisted an alloy formation. More specifically, Pd-rich aerogels showed large monometallic domains that consist of Pd or Pt with sizes of a few up to several tens of nanometers. The Pt-rich aerogel showed a more uniform distribution of Pd and Pt atoms at the nano- and macro-scale. Based on the EXAFS results, only at the Ångstrom-scale we did identify the arrangement of homometallic paired atoms that signify a tendency for clustering of atoms. In addition, the electrochemical stability of the $Pd_{80}Pt_{20}$ aerogel was investigated by using in situ EXAFS. In this work, we provide for the first time in-depth insights into the structure and chemical distributions of the Pd-Pt aerogels prepared by the two-step gelation pro-

cess and discuss the capability of these Pd-Pt aerogels for electrochemical applications.

Results and Discussion

Various architectures of multimetallic aerogels

In the case of the self-assembled bimetallic aerogels prepared by the two-step gelation process, three possible architectures can be formed: (i) nonalloyed, (ii) randomly disordered alloyed (solid solution), and (iii) segregated aerogel nanostructure (Figure 1). The initial nanoparticles are the respective building blocks of the nanochain segments of the aerogel that result in the nonalloyed structure. If surface diffusion processes take place at the interfaces between the linked nanoparticles, the dissimilar atoms can rearrange in this region to form alloyed or core–shell nanochain motifs. The question arises of if the interdiffusion process occurs at the interfaces between the neighboring monometallic platinum and palladium particles during the gelation and how the aerogel structure would change as a result of the high mobility of these dissimilar atoms.
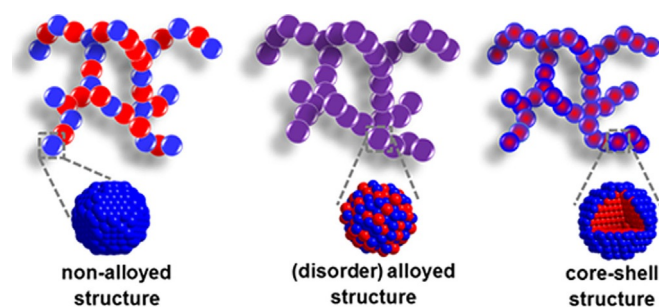

Figure 1. Possible architectures of bimetallic aerogels prepared by the two-step gelation process.

High-resolution transmission electron microscopy

Representative transmission electron microscopy (TEM) images at low and high magnifications of the pristine Pd-Pt aerogels illustrate the typical long-range 3D nanochain-like network structure (Figure 2). The high-magnification TEM images (Figure 2c and 2f) reveal that the diameter of the nanochains varies slightly along their length. The mean diameter of the nanochains was (5.1 ± 1.3) and (3.9 ± 1.1) nm for as-prepared $Pd_{80}Pt_{20}$ and $Pd_{20}Pt_{80}$, respectively. We observed a stronger aggregation of the particles only at the sections at which two or more nanochains cross.

The high resolution TEM micrographs of representative regions of the Pd-Pt aerogels that show single-crystalline domains with their lattice fringes embedded in the nanochains are displayed in Figure S1. Various orientations of the crystallites were observed and indicate the polycrystallinity of the materials. The grain boundaries of the anchored nanoparticles signify no preferred growth direction, which would be expected, for example, for twin growth. We can conclude that the anchoring of nanoparticles was not influenced by the initial orientation of the nanoparticles during the coalescence process.

Bright-field scanning transmission electron microscopy equipped with energy-dispersive X-ray spectroscopy

Representative bright-field scanning transmission electron microscopy (BF-STEM) images and the corresponding EDX maps of the pristine Pd-Pt aerogels are shown in Figure 3. The average Pd/Pt atomic ratios established from these broad regions (Figure 3a and d) at low magnification were 17:83 and 82:18 with an error of 1–2 at% for the $Pd_{20}Pt_{80}$ and $Pd_{80}Pt_{20}$ aerogels, respectively. These values are in good agreement with the original content of pure single Pd and Pt nanoparticles that
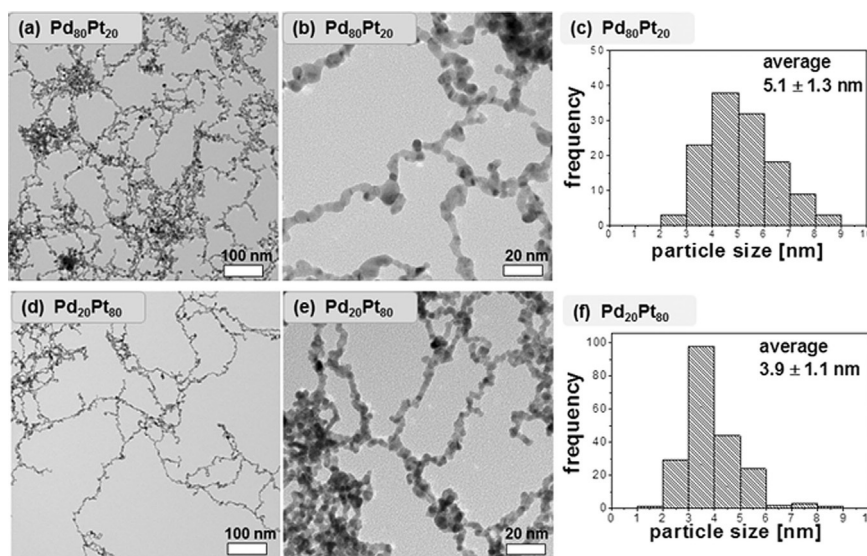

Figure 2. TEM images at a, d) low and b, e) high magnification of the pristine $Pd_{80}Pt_{20}$ and $Pd_{20}Pt_{80}$ aerogels. The mean particle size along the nanochain-based structure was established by counting around 150–200 nanoparticles to result in sizes of (5.1 ± 1.3) and (3.9 ± 1.1) nm for the pristine $Pd_{80}Pt_{20}$ and $Pd_{20}Pt_{80}$, respectively.
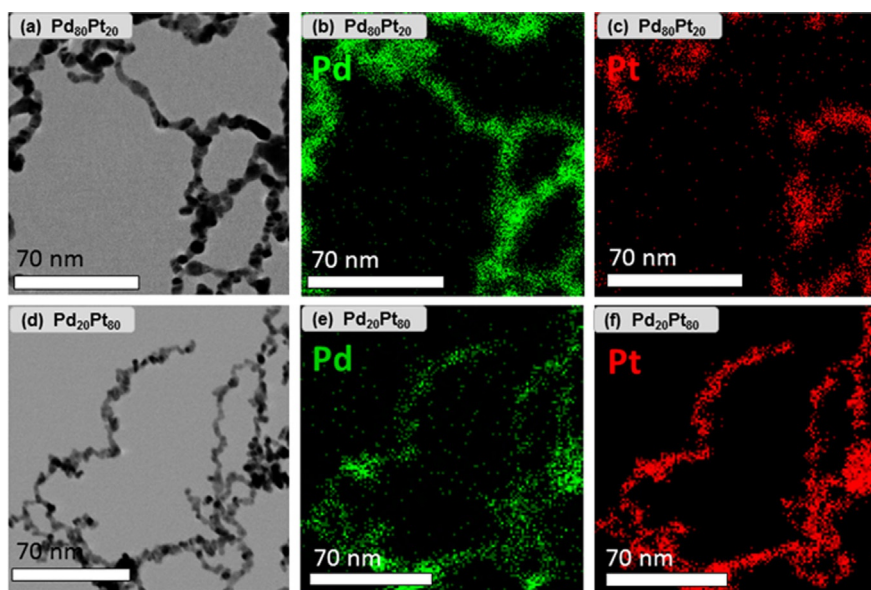
Figure 3. a, d) BF-STEM micrographs combined with EDX maps of the b, e) Pd and c, f) Pt L$_\alpha$-line of the pristine Pd$_{80}$Pt$_{20}$ and Pd$_{20}$Pt$_{80}$ aerogels. The EDX maps of Pd and Pt are displayed in green and red, respectively.

were mixed during the gelation process. We used X-ray photoelectron spectroscopy (XPS) to show that the oxidation states of Pd and Pt inside the aerogels are mainly metallic and only a small content of oxidized Pd was found (Figure S3). This suggests that the chemical composition of the Pd-Pt aerogel networks can be tuned easily by the addition of the desired amount of colloidal metal nanoparticles during the hydrogel synthesis.

Additional EDX mapping and EDX spot analysis with an electron beam spot size of 1.5 nm diameter were performed on both aerogels to clarify the distribution of Pt and Pd atoms inside the nanostructure. In case of the pristine Pd$_{80}$Pt$_{20}$ aerogel (Figure 3b and c), a comparison of the EDX maps of Pd and Pt shows that the Pt atoms are arranged in two different motifs. Pt atoms appear as Pt-rich clusters in the nanochains, and the residual Pt atoms are interfused with Pd atoms to form an alloy. Both motifs (Pt-rich clusters and Pt alloys) are distributed randomly in this framework. To clarify the difference between the Pt-rich clusters and Pt alloys, we define clusters as areas with a strong enrichment of one metal (the fraction of the other metal is less than a few at%), whereas Pt alloys are a mixture of two metals (the fraction of the other metal is larger than 10 at%). The dimensions of the randomly distributed Pt-rich clusters vary significantly from a few up to several tens of nanometers. Additionally, the regions in which a mixture of Pt and Pd was identified ranged from approximately a few up to several tens of nanometers. It is evident that the Pt atoms are not distributed homogeneously over the entire metallic framework. It seems that Pd atoms are better distributed over large regions of the nanochains. Consequently, as a result of the strong appearance of Pt clusters, the aerogel framework exhibited regions that consisted of almost pure Pd. In other words, as fewer Pt atoms are available to form a solid solution with Pd, Pd atoms are also ordered in the form of Pd-

rich clusters. Finally, based on the appearance of large fraction of unalloyed material, the structure of the as-prepared Pd$_{80}$Pt$_{20}$ aerogel looks similar to the postulated structure (Figure 1a).

Representative EDX maps obtained from the pristine Pd$_{20}$Pt$_{80}$ aerogel are shown in Figure 3e and f. A comparison between the EDX maps for Pt and Pd shows a more homogeneous distribution of both metals along the nanochains relative to that of the Pd$_{80}$Pt$_{20}$ material. The presence of large Pt-rich or Pd-rich clusters was not observed at this magnification. It seems that the arrangement of Pt and Pd atoms is a random mixture as postulated in Figure 1b for alloyed aerogels. Notably, the local heterogeneity inside the single nanoparticles along the nanochains by the formation of small clusters of sub-nanometer sizes is very difficult to estimate from EDX maps because of the relatively low lateral resolution of this technique.

EDX spot measurements were conducted to establish the local chemical composition of the unbranched and branched nanochains for the pristine Pd-Pt aerogels shown in Figure S2. The spatial distribution of both metals along the nanochains within the Pd$_{80}$Pt$_{20}$ aerogel showed regions with a very high content of one metal as well as mixed regions with different atomic ratios. Although the EDX map results for the pristine Pd$_{20}$Pt$_{80}$ aerogel (Figure 3e–f) give a strong impression of a homogenous distribution of both metals along the nanochains, the local EDX spot analysis revealed a significant change of the chemical composition from location to location. The variation is not as large (around 10%) as that of the EDX results for the pristine Pd$_{80}$Pt$_{20}$ aerogel. Only few small regions showed a high content of only one metal (see position (2) in Figure S2b). As both metals are largely dispersed along the nanochains, the distribution of the Pd$_{20}$Pt$_{80}$ aerogel is more homogenous than that of the Pd$_{80}$Pt$_{20}$ aerogel. The formation of monometallic clusters with different sizes can be likely explained by the different diffusion coefficients of Pd and Pt surface atoms and/or

the statistical probability, which describes what sort and how frequently initial monometallic nanoparticles collide and fuse to form a nanochain in aqueous media. Further work is in progress to better understand the observed clusters inside the Pd-Pt aerogels.

Ex situ EXAFS spectroscopy

EXAFS spectroscopy measurements were performed on the as-prepared Pd-Pt aerogels to provide an insight into the degree of alloying. The k^2-weighted EXAFS spectra of the Pd-Pt aerogels are plotted with those of the corresponding metal foils at the respective edges (Figure 4a, c, and e). The comparison shows that the k^2-weighted EXAFS data of the Pd-Pt aerogels look similar to the data of the pure Pd or Pt foils. This suggests a characteristic monometallic behavior of Pt and Pd atoms inside the Pd-Pt aerogels.

The k^2-weighted Fourier-transformed EXAFS spectra (black solid lines) and the corresponding best fits (red solid lines) of the pristine $Pd_{80}Pt_{20}$ and $Pd_{20}Pt_{80}$ aerogels are presented in Figure 4b, d, and f. The best-fit parameters of the nearest coordination numbers (N), atomic distances (R), and mean square disorder parameter (σ^2) for the pristine Pd-Pt aerogels are summarized in Table 1. In the case of the $Pd_{80}Pt_{20}$ aerogel, both the spectra at the Pt L_3-edge and Pd K-edge were used for the multi-edge EXAFS fit analysis (Figure 4b and d). The multi-edge EXAFS fit analysis for the $Pd_{80}Pt_{20}$ aerogel revealed that

the peaks in the Fourier-transformed k^2-weighted EXAFS spectra at the Pt L_3-edge and Pd K-edge correspond to the scattering of pairs of Pt—Pt and Pd—Pd atoms in the first shell, respectively, without a detectable contribution of heterometallic Pt—Pd and Pd—Pt bonds. Thus, the $Pd_{80}Pt_{20}$ aerogel shows a strong monometallic behavior in the local coordination environment, which indicates the formation of Pd-rich and Pt-rich clusters within the aerogel framework. Similar multi-edge EXAFS fit results were obtained for the pristine $Pd_{50}Pt_{50}$ aerogel.[1k] In both Pd-Pt aerogels, the Pd-rich and Pt-rich clusters prevail over the features of Pd-Pt alloys.

As the sum of all partial coordination shells corresponds to the total coordination shell of each metal, the values of the total coordination shell for Pd and Pt atoms are lower than that for the macroscopic (bulk) counterparts ($N_{total} = 12$), which indicates that the aerogels exhibit nanoparticle-like characteristics. The values of the total coordination shell for the Pd and Pt atoms are similar, which signifies that the particle sizes of the pure Pt and Pd nanoparticles are almost equal. This observation is consistent with the results obtained by using TEM [Figure 2; $d_{avg} = (5.1 \pm 1.3)$ and (3.9 ± 1.1) nm for $Pd_{80}Pt_{20}$ and $Pd_{20}Pt_{80}$, respectively].

The k^2-weighted Fourier-transformed EXAFS spectra of the pristine $Pd_{20}Pt_{80}$ aerogel recorded at the Pt L_3-edge are shown in Figure 4f. The best fit for this aerogel (Table 1) indicates the presence of a homometallic bond (Pt—Pt) in the first shell. Although the $Pd_{20}Pt_{80}$ aerogel showed a better homogeneity
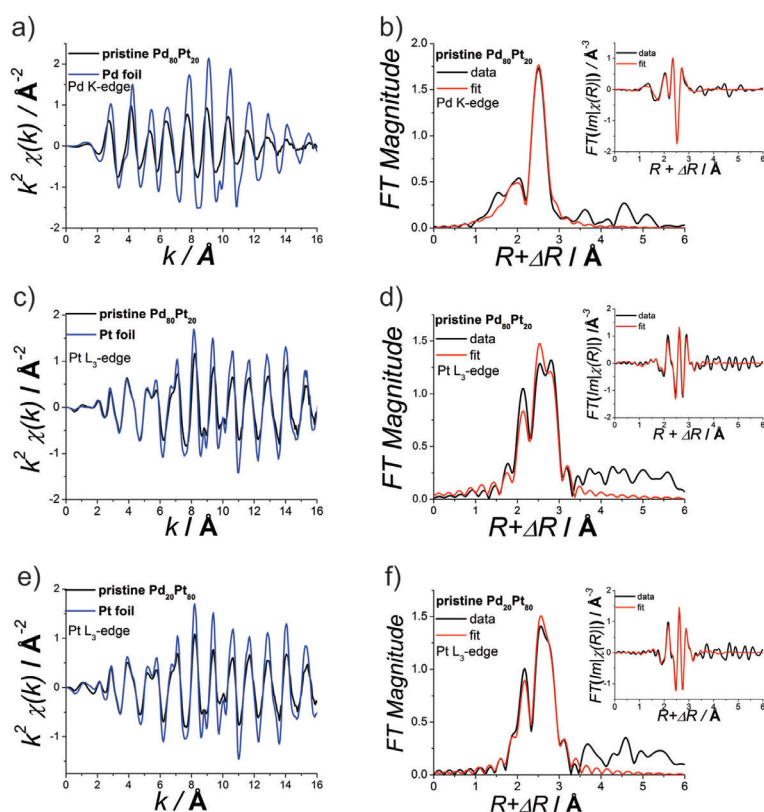

Figure 4. a, c, e) k^2-weighted Pd K-edge and Pt L_3-edge EXAFS data and b, d, f) the corresponding Fourier-transformed EXAFS data for the pristine $Pd_{80}Pd_{20}$ and $Pd_{20}Pt_{80}$ aerogels. The inset plots in b, d, and f show the imaginary part of the k^2-weighted Fourier-transformed EXAFS spectra (black lines) and the corresponding fits (red lines).

Table 1. First nearest neighbor coordination shell (N), atomic distance (R), mean square disorder parameter (σ^2), energy shift (ΔE_0) at the corresponding edges, and R_f factor (closeness of the fit as quality parameter) for the pristine $Pd_{80}Pt_{20}$ and $Pd_{20}Pt_{80}$ aerogels prepared by the two-step gelation process.

	Shell/phase	N	R [Å]	$\sigma^2 \times 10^{-4}$ [Å^2]	ΔE_0 [eV]	R_f
$Pd_{80}Pt_{20}$	Pt-Pt$_1$/$Fm\bar{3}m$	9.4 ± 1.2	2.759 ± 0.004	53 ± 5	7.9 ± 0.9	0.0127
	Pd-Pd$_1$/$Fm\bar{3}m$	9.2 ± 0.8	2.789 ± 0.005	89 ± 7	-8.1 ± 0.6	
$Pd_{20}Pt_{80}$	Pt-Pt$_1$/$Fm\bar{3}m$	9.1 ± 0.6	2.756 ± 0.003	55 ± 3	7.7 ± 0.6	0.0043

The mean values of the ECSA were (66 ± 3) and (52 ± 8) m^2 g$_{metal}^{-1}$ for the $Pd_{20}Pt_{80}$ and $Pd_{80}Pt_{20}$, respectively. The resulting ECSA values are almost comparable to that of commercially available Pt nanoparticles supported on high-surface-area carbon.[13a, 15] As the ECSA values are similar to the BET values, it appears that a large fraction of the surface of the bimetallic aerogels is free from impurities. In principle, the total surface area should be catalytically active for the electrochemical activation of small molecules
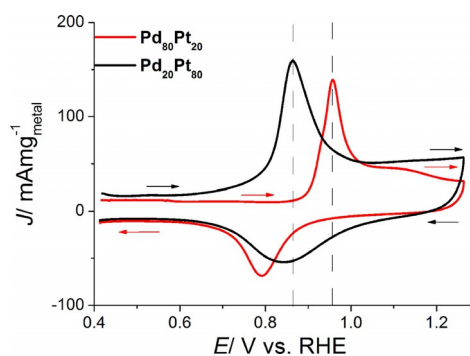
within the nanochains at the few nanometer scale established by using STEM-EDX, the EXAFS results clearly revealed the homometallic pairing features at the Ångstrom-scale. Consequently, we can conclude that Pd atoms are largely paired with Pd atoms in the first shell. Notably, the features of the homoatomic pairing were only observed by using Ångstrom-resolved EXAFS. At large length scales, both metals, Pd and Pt, show an even distribution over the whole aerogel structure.

In summary, different techniques were used in this work to identify the structure, chemical distribution, and homogeneity of the self-assembled Pd-Pt aerogels prepared by the two-step gelation process. The Pd-Pt aerogels that consist of a finite plurality of connected single nanoparticles showed a highly complex structure with regard to the homogeneity and chemical distribution. With this preparation method, the coalescence of monometallic Pt and Pd nanoparticles leads to a chemically heterogeneous structure, in which the original cluster motif dominates fully over alloying as illustrated in Figure 1 a. The presence of monometallic domains inside the aerogel indicates that the diffusion kinetics of the Pd and Pt atoms at ambient and low temperatures are very slow. Further studies are required to better understand the two-step gelation process, its reproducibility, and the interdiffusion kinetics for the Pd-Pt aerogel system.

Electrochemically active surface area measurements

We chose to determine the electrochemically active surface area (ECSA) of the Pd-Pt aerogels by using the CO stripping method as the typical underpotential hydrogen deposition (H_{upd}) method is inappropriate for Pd-based materials because of the formation of absorbed hydrogen.[14] The CO stripping profiles of both aerogels in 0.1 M HClO$_4$ are shown in Figure 5. The large anodic current peak is associated with the electrochemical oxidation of the adsorbed CO monolayer to water and CO$_2$. The potentials at the current maxima are around 0.86 and 0.96 V versus the reversible hydrogen electrode (RHE) for the $Pd_{20}Pt_{80}$ and $Pd_{80}Pt_{20}$ aerogels, respectively. We suggest that the effects of the size of the nanochains are likely negligible as the average diameter of both aerogels is similar. Therefore, a shift of the CO-stripping peak is largely related to the chemical composition of the surface and subsurface. The observed broad and slightly irregular CO stripping peak is affected by the local variation of the surface composition of the bimetallic aerogels.

Figure 5. CO-stripping CV profiles of the pristine $Pd_{80}Pt_{20}$ (red line) and $Pd_{20}Pt_{80}$ (black line) aerogels. Experimental parameters: scan rate of 50 mV s^{-1}, metal loading of 12–17 μg cm^{-2} (geometric) in 0.1 M HClO$_4$ at room temperature. The arrows indicate the scan direction.

such as oxygen. Therefore, we tested these aerogels for the electrocatalytic oxygen reduction reaction (ORR) in acidic media. Unfortunately, the Pd-Pt aerogels prepared by the two-step gelation process showed a poor catalytic performance (not shown). This poor reactivity was likely correlated with the structural inhomogeneity of these materials. Possible strategies to improve the distribution and hence the catalytic properties of these aerogels would be the modification of synthesis parameters (e.g., by changing the temperature or using smaller nanoparticles) and/or thermal post-annealing.

Electrochemical short-term durability tests of the $Pd_{80}Pt_{20}$ and $Pd_{20}Pt_{80}$ aerogels

An accelerated cyclic voltammetry test protocol was applied to analyze the durability of the Pd-Pt aerogels in the potential range of 0.5–1.5 V vs. RHE at 50 mV s^{-1} in N$_2$-saturated 0.1 M HClO$_4$ at room temperature. During the run, after a certain number of cycles CO stripping profiles were recorded to monitor the changes of the ECSA. The dependence of the ECSA on the cycle number for the $Pd_{80}Pt_{20}$ and $Pd_{20}Pt_{80}$ aerogels after potential cycling (0.5–1.5 V vs. RHE) is shown in Figure 6. Clearly, for the $Pd_{80}Pt_{20}$ aerogel (Figure 6 a) the CO stripping current peak decreased drastically and shifted to lower anodic potentials with the increasing cycle number. The shift of the CO stripping peak is likely related to the surface enrichment of Pt in the aerogel by electrochemical dissolution of Pd and/or by increase of the particle size (e.g., Ostwald ripening). It is well
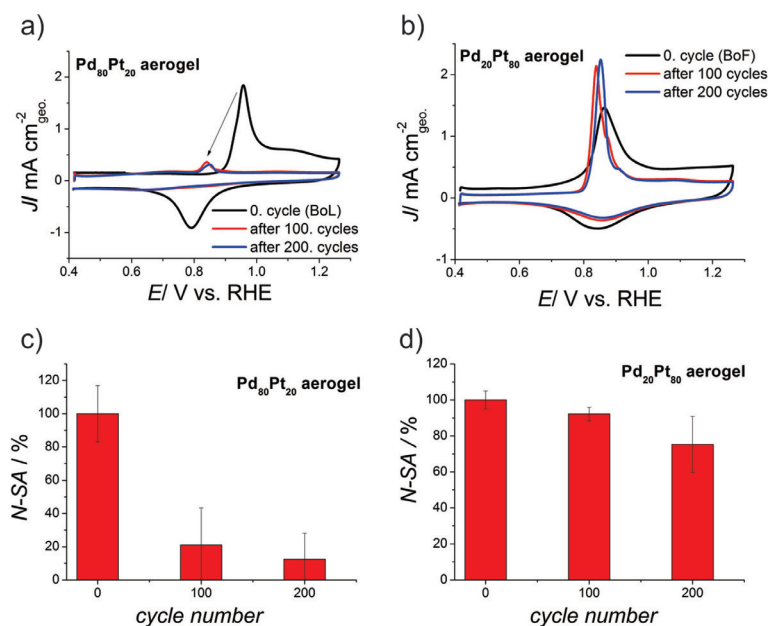
Figure 6. a, b) CO-stripping CV profiles of Pd-Pt aerogels after a 0, 100, and 200 cycles between 0.5 and 1.5 V vs. RHE at 50 mV s^{-1} in N$_2$-saturated 0.1 M HClO$_4$. The calculated loadings were in the range of 10–17 µg cm^{-2} (metal). c–d) Dependence of the loss of the normalized SA loss on the cycle number induced by electrochemical cycling up to 1.5 V vs. RHE.

known that with an increasing particle size the oxophility of the Pt particles decreases to result in a shift of the CO stripping current peak to higher anodic potentials.[12] The electrochemically active surface area (SA) (not normalized to the used mass of aerogel) was estimated from the CO stripping peak and normalized to the initial SA value (beginning-of-life). The dependence of the normalized SA values on the cycle number is shown in Figure 6c and d. For the Pd$_{80}$Pt$_{20}$ aerogel, the SA decreased to below 20% after 200 cycles between 0.5 and 1.5 V vs. RHE, which results from the strong depletion of Pd. It is assumed that the drastic decrease of SA for the Pd$_{80}$Pt$_{20}$ aerogel is caused by the high content of Pd as well as the strong heterogeneity observed by using STEM-EDX and EXAFS (Figures 3 and 4). In particular, regions of the nanochains that contain a high Pd content became very unstable at high anodic potentials. It seems that during the backward scan most of the Pd ions in the electrolyte were not redeposited on the aerogel surface. The large error bars shown in Figure 6c were established from five independent rotating disc electrode (RDE) measurements. The relatively large error bars are likely related to the very rapid depletion of Pd in this potential range and the chemical heterogeneity of the aerogel. Altogether, the existence of large Pd-enriched regions mainly destabilized the entire aerogel network, which makes it unsuitable for fuel cell applications. To date, it is not clear how the electrochemical dissolution process of Pd occurs during the potential cycling. Several studies on polycrystalline Pd showed that in the anodic scan the Pd had already formed surface oxides at low potentials relative to the standard potential in acidic media.[16] The thickness of Pd oxide layers increased with the increasing upper potential, however, at high upper potentials the electrochemically preformed palladium oxide commenced to dissolve in the anodic scan. Nevertheless, most of the palladium oxide

dissolved electrochemically in the backward scan before soluble Pd species could be reduced to metallic Pd. Similar electrochemical dissolution behavior was observed for Pt. The electrochemical dissolution mechanisms for macroscopic metal electrode surfaces have been studied comprehensively by many groups.[17] They showed that the electrochemical dissolution rate of polycrystalline Pt is pronounced at the transition state between oxidation and reduction processes. For instance, if the Pt surface is electrochemically oxidized by increasing the anodic potential (larger than 1.2 V vs. RHE), the backward (cathodic) scan causes an acceleration of the dissolution process of an oxidized Pt surface. In contrast, during the anodic scan the dissolution rate of metallic Pt is almost negligible. As Pd is less noble and thus exhibits a more oxophilic behavior, we suggest that the electrochemical dissolution of Pd occurs much more easily than that of Pt.

The CO stripping profiles of the Pd$_{20}$Pt$_{80}$ aerogel after a certain number of cycles from 0.5 and 1.5 V vs. RHE with 50 mV s^{-1} are shown in Figure 6b. The shift of the CO stripping current peak to lower anodic potentials was very small. Only the comparison of the shape of the CO stripping current peak exhibited a significant change before and after electrochemical cycling. After 100 cycles, the CO stripping current peak became clearly narrower, which indicates an improved distribution of the sizes of the nanochains or of the chemical surface composition inside the treated aerogel. The dependence of the SA on the cycle number is shown in Figure 6d. Notably, the SA decreased only by 25%. The unsupported Pd$_{20}$Pt$_{80}$ aerogel exhibited a considerable electrochemical durability. Many studies on carbon-supported Pt nanoparticles (Pt/C) showed a loss of ECSA of around 40–50% under similar conditions.[13a, e] The large loss of the ECSA for Pt/C is associated with carbon corrosion, dissolution of small nanoparticles, and particle de-

tachment. The improved stability of the $Pd_{20}Pt_{80}$ aerogel observed experimentally was largely caused by the higher content of Pt and the absence of a carbon support material.

Structural stability of the $Pd_{80}Pt_{20}$ aerogel probed by using in situ electrochemical EXAFS

As the $Pd_{80}Pt_{20}$ aerogel showed the largest alteration during the electrochemical cycling, in situ EXAFS studies were performed to better understand its aging. During the EXAFS measurements, the aerogel-coated working electrode was under potential control and was held at 0.5 V vs. RHE. This potential is in the electrochemical double layer regime of both metals and decreases the electrochemical formation of oxygen-containing species on the aerogel surface. In other words, in the double layer regime, the surface of both metals should mainly exist in the metallic state.

The in situ k^2-weighted Fourier-transformed EXAFS spectra (black lines) and the corresponding best fits (red lines) for the $Pd_{80}Pt_{20}$ aerogel recorded at the Pd K-edge and by holding the potential of 0.5 V vs. RHE after a certain number of cycle (0.5–1.5 V vs. RHE) is shown in Figure 7a. The best-fit parameters for the first shell of the treated $Pd_{80}Pt_{20}$ aerogel are summarized in Table 2. The behavior of the coordination numbers for the Pd-Pd, Pd-Pt, and Pd-M (M=Pt, Pd) pairs versus the cycle number is plotted in Figure 7c.

After the electrochemical cleaning process (0.35–1.2 V vs. RHE with 50 mV s^{-1}, 10 cycles), we observed the presence of a Pd-Pt scattering pair in the $Pd_{80}Pt_{20}$ aerogel. After 10 potential cycles, N(Pd-Pt) is around (2.3 ± 1.0), whereas N(Pd-Pd) de-

creased from (9.0 ± 0.7) to (7.1 ± 1.0) (a change of around 23%). The evolution of Pd-Pt atom pairs is largely related to the rearrangement of the particle surface by electrochemical redissolution and the redeposition of Pt and Pd atoms from the electrolyte or by the surface diffusion of Pd and Pt atoms to form a Pd-Pt alloy. Generally, low coordination numbers are largely associated with surface atoms because of the absence of additional atoms compared to the corresponding atoms in the bulk. A comparison of N(Pd-Pt) and N(Pd-Pd) indicates that Pt atoms exist at the surface of the aerogel or that the Pd atoms preferred to deposit on Pt-rich clusters. Both processes can form an alloy at the surface or at the solid–solid interface. As Pt is more electrochemically stable than Pd, we suggest that the surface of the aerogel is enriched gradually with Pt. The gradual increase of the amount of Pt atoms on the surface and subsurface was also inferred from the results of the CO stripping experiments (Figure 6a). The gradual accumulation of Pt atoms at the surface may protect the residual Pd atoms from further electrochemical dissolution.

The change of the total coordination number, which can be estimated from the sum of N(Pd-Pt) and N(Pd-Pd), during the experiment (Figure 7c). N(Pd-M) was almost stable over the potential cycling test protocol (before and after 200 cycles), and the total coordination numbers did not change within the experimental uncertainties, (9.3 ± 0.7) and (9.6 ± 1.2), respectively, which indicates that the diameter size of the nanochains seems to be almost unchanged. Notably, a change of the total coordination number of the adsorbing Pd atom would drastically affect the particle size. Figure 7d visualizes the structural changes of the Pd-rich aerogel by the dissolution of Pd and enrichment of Pt induced by electrochemical cycling.

We want to emphasize that these in situ EXAFS results involve only information about the local structural changes of Pd atoms inside the $Pd_{80}Pt_{20}$ aerogel during the aging process. The observed features for the Pd-rich aerogel constitute only a glimpse of the structural durability induced by electrochemical cycling. Nevertheless, the in situ EXAFS results provide new insights into the electrochemical aging process of the new Pd-rich aerogel.

Conclusions

We investigated comprehensively the structure and chemical composition of $Pd_{80}Pt_{20}$ and $Pd_{20}Pt_{80}$ aerogels prepared by a two-step gelation process. We used extended X-ray absorption fine structure (EXAFS) spectroscopy and (scanning) transmission electron microscopy with energy-dispersive X-ray spectroscopy (STEM-EDX) to identify the final structure and chemical distribution for both aerogels at different length scales. It was evident that the Pd/Pt-rich clusters that originate from the initial nanoparticles prevail over the alloy formation. The size of the monometallic domains varied strongly between the Pd-Pt aerogels. For instance, the Pd-rich aerogel showed a stronger chemical heterogeneity because
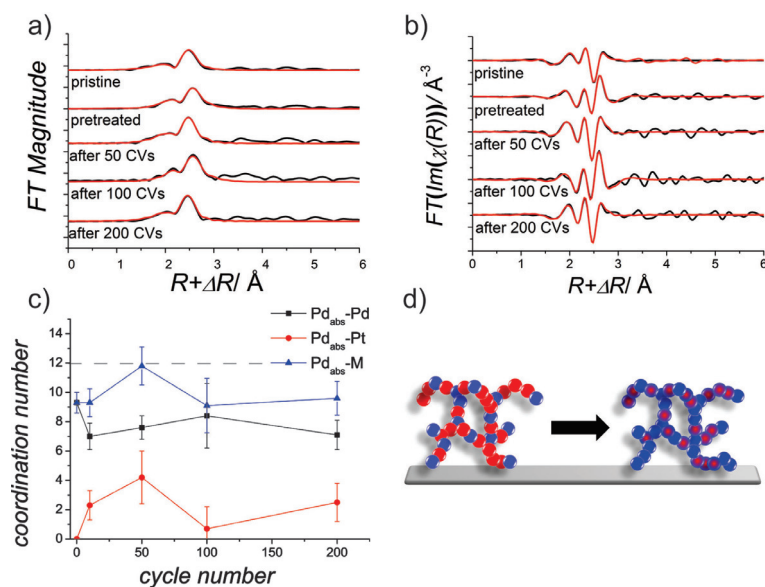

Figure 7. a) In-situ k^2-weighted Fourier-transformed EXAFS spectra (black lines) and the corresponding fits (red lines) for the $Pd_{80}Pt_{20}$ aerogel at the Pd K-edge recorded after a certain number of cycles in the potential range of 0.5 and 1.5 V vs. RHE at 50 mV s^{-1} in N_2-saturated 0.1 M $HClO_4$. b) Imaginary part of the k^2-weighted Fourier-transformed EXAFS spectra (black lines) and the corresponding fits (red lines). c) Dependence of the evolution of the coordination number for the paired atoms (Pd–Pd, Pd–Pt, and Pd–M) on the number of cycles for the $Pd_{80}Pt_{20}$ aerogel. d) Illustration of the aging process of the $Pd_{80}Pt_{20}$ aerogel induced by electrochemical cycling.

Table 2. First nearest neighbor coordination number (N), total Pd metal coordination number ($N_{\text{Pd-M}}$), atomic distances (R), mean square disorder parameter (σ^2), energy shift (ΔE_0) at the Pd K-edge, and R_f factor for the electrochemically treated $Pd_{80}Pt_{20}$ aerogel.

Cycle number	Shell/ phase	N	R [Å]	$\sigma^2 \times 10^{-4}$ [Å²]	ΔE_0 [eV]	R_f
0 = as-prepared	Pd-Pd$_1$/$Fm\bar{3}m$	9.3 ± 0.7	2.767 ± 0.005	88 ± 5	−7.9 ± 0.5	0.0070
10 = pretreated	Pd-Pd$_1$/$Fm\bar{3}m$	7.0 ± 0.9	2.748 ± 0.008	70 ± 12	2.0 ± 0.6	0.0015
	Pd-Pt$_1$/$Fm\bar{3}m$	2.3 ± 1.0	2.710 ± 0.025	66 ± 30		
	Pd-M/$Fm\bar{3}m$	9.3 ± 1.0				
50	Pd-Pd$_1$/$Fm\bar{3}m$	7.6 ± 0.8	2.734 ± 0.006	59 ± 8	−5.0 ± 0.6	0.0012
	Pd-Pt$_1$/$Fm\bar{3}m$	4.2 ± 1.8	2.713 ± 0.023	97 ± 49		
	Pd-M/$Fm\bar{3}m$	11.8 ± 1.3				
100	Pd-Pd$_1$/$Fm\bar{3}m$	8.4 ± 2.2	2.744 ± 0.013	60 ± 19	4.1 ± 1.2	0.0098
	Pd-Pt$_1$/$Fm\bar{3}m$	0.7 ± 1.5	2.723 ± 0.020	11 ± 51		
	Pd-M/$Fm\bar{3}m$	9.1 ± 1.8				
200	Pd-Pd$_1$/$Fm\bar{3}m$	7.1 ± 1.0	2.734 ± 0.009	54 ± 10	−7.5 ± 0.9	0.0034
	Pd-Pt$_1$/$Fm\bar{3}m$	2.5 ± 1.3	2.705 ± 0.023	60 ± 31		
	Pd-M/$Fm\bar{3}m$	9.6 ± 1.1				

of the presence of large Pd/Pt-rich clusters with a size of several tens of nanometers. In contrast, STEM-EDX revealed a more homogeneous distribution of Pd and Pt atoms inside the $Pd_{20}Pt_{80}$ aerogel at a larger length scale. The EXAFS investigations showed features of homoatomic pairing (Pd-Pd and Pt-Pt) in the first coordination shell, which indicates clusters at the local-scale. Therefore, the $Pd_{20}Pt_{80}$ aerogel showed a higher structural and chemical homogeneity than the $Pd_{80}Pt_{20}$ aerogel.

In addition, the CO stripping experiments revealed that the electrochemically active surface areas of the Pd–Pt aerogels are similar to the BET surface areas evaluated by using physisorption, which shows that the aerogel surfaces were free of impurities, such as organic ligands, and showed a high accessibility for the electrocatalytic conversion of small molecules. However, to improve the electrocatalytic performance, a better homogeneity and chemical distribution of the bimetallic aerogel are still necessary.

The accelerated degradation test protocol showed that, in particular, Pd-rich clusters inside the $Pd_{80}Pt_{20}$ aerogel strongly suffered during the electrochemical cycling. Significant changes of the structure and chemical composition induced by electrochemical cycling were monitored in situ by using EXAFS and CO stripping experiments. Thereby, the Pd-rich aerogels showed a lower electrochemical stability than the Pt-rich aerogels. The pronounced aging process of the Pd-rich aerogels is based on the successive electrochemical dissolution of Pd, in particular the strong depletion of Pd from the Pd-rich clusters. To increase the robustness of Pd-rich aerogels, the surface and subsurface structure and composition need to be homogeneous and uniform.

The homogeneity of an aerogel is important to stabilize the long-range network structure. In particular, regions with a higher content of a less noble metal can be dissolved easily under electrochemical conditions, and hence the aerogel displays so-called "weak spots" at which the electrochemical degradation process takes place drastically. Therefore, the control of the structure and chemical distribution of the dissimilar metal atoms inside the short-range of the nanochains as well as inside the long-range of the aerogel framework during the two-step gelation process is crucial.

Experimental Section

Gelation and formation of various bimetallic Pt-Pd aerogels

Aqueous colloidal solutions of monometallic Pt and Pd nanoparticles were prepared separately (Supporting Information). We used $H_2PtCl_6 \cdot 6\,H_2O$ ($\geq 99.95\,\%$, Sigma Aldrich) and $PdCl_2$ ($99.999\,\%$ Sigma Aldrich) as precursor salts. The atomic ratio of Pd/Pt was varied between 4:1 and 1:4, and the gel formation took place at 348 K and was stopped after 5 and 10 h, respectively, when the supernatant above the hydrogel became a clear solution. The transformation of the hydrogel to solid aerogel without a significant loss of porosity was performed by using a supercritical dryer with liquid CO_2 (13200J-AB, SPI Supplies). After drying, the Pd-Pt aerogels appeared as black monoliths and were stored at RT in air.

HR(S)TEM-EDX

The TEM measurements were performed by using a ZEISS LIBRA 200 microscope. The microscope was operated at an acceleration voltage of 200 kV. The TEM images were acquired by using iTEM Software. The samples were prepared by dispersing the aerogels in methanol. The aerogel dispersion was dropped onto a copper grid coated with a thin Formvar-carbon film and dried at RT in air. The mean diameters of the nanochains of the Pt-Pd aerogels were established by using iTEM 5.2 Software (Olympus Soft Imaging Solutions GmbH).

HR(S)TEM-EDX investigations were performed by using a JEOL JEM2100F. The acceleration voltage of the microscope was 200 kV. The EDX maps of Pd and Pt in the aerogels were measured and analyzed by using the Oxford INCA Energy TEM250 Software. For the EDX mapping, the characteristic energy intensities of the L$_\alpha$-line for Pd and for Pt were evaluated, respectively. EDX spot measurements were performed with an electron beam spot size of 1.5 nm

diameter in the STEM mode and an acquisition time of around 60 s.

EXAFS spectroscopy

EXAFS spectroscopy was performed by using the X10DA (Super-XAS) beamline at the Swiss Light Source (SLS). The storage ring was operated at a beam current of 400 mA and at 2.4 GeV. EXAFS spectra were recorded at the Pt L_3- and Pd K-edges for Pd-Pt aerogels in transmission mode. Incident (I_0) and transmitted (I_1 and I_2) X-rays were detected by ionization chambers filled with Ar for the Pd K-edge measurements. The lengths of the ionization chambers for the incident and transmitted X-rays were 15 and 30 cm, respectively. Similar ionization chambers were used for the Pt L_3-edge measurements, however, the ionization chambers were filled with N_2. EXAFS data reduction and analysis was performed by using IFEFFIT.[9] Preliminary data processing included background subtraction and edge-step normalization. The energy axis [eV] was converted to photoelectron wave number k units [Å^{-1}] by assigning the origin, E_0, to the first inflection point of the absorption edge. The resulting $\chi(k)$ functions were weighted with k^2 to compensate for the dampening of the XAFS amplitude with increasing k and were, subsequently, Fourier-transformed to obtain pseudo-radial structure functions (RSFs). The fitting of the experimental data was done by using a nonlinear least squares Levenberg–Marquardt method.

Ex situ EXAFS spectroscopy

Solid aerogel samples were prepared as pellets by using cellulose as a binder. The EXAFS spectra of the Pt and Pd absorption edges were then analyzed concurrently by applying several constraints between fitting parameters. In the fits, the interatomic distances (R) and the mean square disorder parameters (σ^2) of the heterometallic bonds Pt-Pd and Pd-Pt (as measured from the Pt and Pd absorber perspectives, respectively) were constrained to be equal to each other. Pure Pt and Pd foils were used as reference to establish the amplitude reduction factors for Pd and Pt. By fitting the bulk metals that possess a fcc structure, the coordination number of the first nearest neighbor (Pt—Pt or Pd—Pd) bonds were fixed at 12, and the amplitude reduction factors (S_0^2) for Pd and Pt were varied. The final S_0^2 values obtained were 0.83 and 0.91 for Pt and Pd, respectively, and were then fixed to these values in the fits of the aerogel EXAFS data. For that, the theoretical scattering paths of all pairs (Pt-Pt, Pt-Pd, Pd-Pt, and Pd-Pd) were calculated using the fcc structure in which some atoms in the nearest-neighbor positions were replaced with the other metal.

In situ electrochemical EXAFS spectroscopy

A home-made spectroelectrochemical PEEK cell with Kapton windows and three electrodes was employed to investigate the changes of the aerogel structures in an electrochemical environment. A gold wire and a mercury-mercury sulfate (MMS) electrode were used as the counter and reference electrode, respectively. 0.1 M HClO$_4$ was used as the electrolyte solution. For the preparation of the working electrode (WE), a dispersion that consisted of an aerogel/water/iso-propanol/Nafion mixture (described below) was dropped onto a carbon paper and dried at around 40 °C in air. The calculated metal loading was around 100 µg cm^{-2} (geometric). Before the EXAFS spectroscopy commenced, an electrochemical pretreatment of the WE was performed to remove any impurities

and oxygen-containing surface species from the aerogel film and/or carbon paper. The WE was pretreated electrochemically in a potential range of 0.35–1.20 V vs. RHE at a scan rate of 50 mV s^{-1} in 0.1 M HClO$_4$. Afterwards, the WE was assembled into the cell. The WE was cycled electrochemically in the range of 0.5–1.5 V vs. RHE at a scan rate of 50 mV s^{-1}. During the run, after 50, 100, and 200 potential cycles, in situ EXAFS spectra (three scans) were recorded from the aerogel samples at a constant potential of 0.5 V vs. RHE.

Electrochemical characterization by using the thin-film RDE technique

Preparation of the working electrode

The aerogel (1–2 mg) was added to a 5.00 mL solution that consisted of water (3.98 mL), iso-propanol (1.00 mL), and Nafion (20 µL of 5 wt% Nafion solution). After horn-sonication (Hielscher UP200H, Germany) for 30 min, 10 µL of the dispersion was pipetted onto the pre-cleaned and mirror-like surface of a glassy carbon (GC) electrode (with an outer diameter of 5 mm) embedded in Teflon (supplied by PINE, USA). The coated electrode was dried for 20–25 min at 40 °C in air to result in a thin homogenous film. The calculated total metal loading of the WE was 10–20 µg$_{metal}$ cm^{-2} (geometric). The GC electrode was polished with 0.3 and 0.05 µm Al$_2$O$_3$ suspension on Microcloth polishing paper (supplied by Prüfmaschine AG, Switzerland).

Electrochemical cyclic voltammetry experiments

All electrochemical measurements were performed by using a home-made three-compartment electrochemical glass cell by using the thin-film RDE technique.[10] The cell was equipped with a rotator (supplied by PINE, USA) and a potentiostat (Biologic, France). The electrochemical glass cell was cleaned in a "piranha" solution (a mixture of 3/4 H$_2$SO$_4$ (96–98%) and 1/4 H$_2$O$_2$ (30%)) overnight and then washed with purified water (18.2 MΩ cm at RT) several times. A three-electrode configuration was used that consisted of a gold wire as the counter electrode, a MMS electrode (supplied by Biologic, France) or Hydroflex (supplied by Gaskatel, Germany) as the reference electrode, and the aerogel-coated thin-film GC electrode as the WE. The reference electrode was held in place by a Luggin–Haber capillary, and the opening of the capillary was positioned below the center of the WE at a distance of around 3 mm. The 0.1 M HClO$_4$ electrolyte solution was freshly prepared by dilution of a 70% suprapure HClO$_4$ (supplied by VWR). The quality of N$_2$ and CO (supplied by Messer) was 5.0 and 4.5, respectively.

Determination of the ECSA by using the CO-stripping method

The WE was immersed into the electrolyte solution (0.1 M HClO$_4$) under potential control and with a rotation speed of 1600 rpm. The potential of the WE was held at 0.1 V vs. RHE during saturation with CO and N$_2$. The CO gas was bubbled through the frits into the electrolyte for 8 min. Then, the electrolyte was saturated with N$_2$ for 25 min to remove the excess dissolved CO from the electrolyte. Afterwards, three cyclic voltammogram (CV) profiles were recorded with a scan rate of 50 mV s^{-1} between 0.35 and 1.2 V vs. RHE.

For the determination of the ECSA, the first CV profile showing the oxidation peak of the adsorbed CO monolayer was subtracted from the second CV profile to take into account the adsorption of anions (OH$^-$, ClO$_4^-$) on the aerogel surface between 0.4 and 1.2 V

vs. RHE. The ECSA was estimated by using the CO stripping peak by assuming a charge of 415 µC cm$_{real}^{-2}$ for a Pd$_{50}$Pt$_{50}$ system to oxidize one CO monolayer. The pseudocapacities for the Pd-Pt aerogels were weighted from the values of pure Pt (420 µC cm^{-2})[11] and Pd (410 µC cm^{-2})[12] surfaces, respectively. All potentials are reported with respect to the RHE.

Electrochemical degradation measurements

An accelerated electrochemical degradation experiment was performed on the aerogels to investigate their electrochemical durability under harsh conditions. Potential cycling between 0.5 and 1.5 V vs. RHE is often applied to examine the electrochemical resistance of metal nanoparticles and support materials for fuel cell applications.[13] The CV profiles were recorded between 0.5 and 1.5 V vs. RHE at a scan rate of 50 mV s^{-1} in N$_2$-saturated 0.1 M HClO$_4$. After 100 and 200 potential cycles, the ECSA was determined by using the CO-stripping method. In between, the electrolyte was removed and refilled with a fresh 0.1 M HClO$_4$ to eliminate any impurities that could be formed during the potential cycling up to 1.5 V vs. RHE (e.g., the decomposition of the electrolyte).

Acknowledgements

[1] a) M. Oezaslan, W. Liu, M. Nachtegaal, A. I. Frenkel, B. Rutkowski, M. Werheid, A. K. Herrmann, C. Laugier-Bonnaud, H. C. Yilmaz, N. Gaponik, A. Czyrska-Filemonowicz, A. Eychmuller, T. J. Schmidt, *Phys. Chem. Chem. Phys.* **2016**, *18*, 20640–20650; b) W. Liu, P. Rodriguez, L. Borchardt, A. Foelske, J. Yuan, A.-K. Herrmann, D. Geiger, Z. Zheng, S. Kaskel, N. Gaponik, R. Kötz, T. J. Schmidt, A. Eychmüller, *Angew. Chem. Int. Ed.* **2013**, *52*, 9849–9852; *Angew. Chem.* **2013**, *125*, 10033–10037; c) W. Liu, A.-K. Herrmann, D. Geiger, L. Borchardt, F. Simon, S. Kaskel, N. Gaponik, A. Eychmüller, *Angew. Chem. Int. Ed.* **2012**, *51*, 5743–5747; *Angew. Chem.* **2012**, *124*, 5841–5846; d) W. Liu, A.-K. Herrmann, N. C. Bigall, P. Rodriguez, D. Wen, M. Oezaslan, T. J. Schmidt, N. Gaponik, A. Eychmüller, *Acc. Chem. Res.* **2015**, *48*, 154–162; e) A.-K. Herrmann, P. Formanek, L. Borchardt, M. Klose, L. Giebeler, J. Eckert, S. Kaskel, N. Gaponik, A. Eychmüller, *Chem. Mater.* **2014**, *26*, 1074–1083; f) N. Gaponik, A.-K. Herrmann, A. Eychmüller, *J. Phys. Chem. Lett.* **2012**, *3*, 8–17; g) H. D. Gesser, P. C. Goswami, *Chem. Rev.* **1989**, *89*, 765–788; h) C. Zhu, D. Du, A. Eychmüller, Y. Lin, *Chem. Rev.* **2015**, *115*, 8896–8943; i) C. Zhu, D. Wen, S. Leubner, M. Oschatz, W. Liu, M. Holzschuh, F. Simon, S. Kaskel, A. Eychmuller, *Chem. Commun.* **2015**, *51*, 7851–7854; j) C. Zhu, D. Wen, M. Oschatz, M. Holzschuh, W. Liu, A.-K. Herrmann, F. Simon, S. Kaskel, A. Eychmüller, *Small* **2015**, *11*, 1430–1434; k) L. Kühn, A.-K. Herrmann, B. Rutkowski, M. Oezaslan, M. Nachtegaal, M. Klose, L. Giebeler, N. Gaponik, J. Eckert, T. J. Schmidt, A. Czyrska-Filemonowicz, A. Eychmüller, *Chem. Eur. J.* **2016**, *22*, 13446–13450.

[2] a) A. Bonakdarpour, J. Wenzel, D. A. Stevens, S. Sheng, T. I. Monchesky, R. Lobel, R. T. Atanasoski, A. K. Schmoeckel, G. D. Vernstrom, M. K. Debe,

J. R. Dahn, *J. Electrochem. Soc.* **2005**, *152*, A61; b) M. K. Debe, A. K. Schmoeckel, G. D. Vernstrom, R. Atanasoski, *J. Power Sources* **2006**, *161*, 1002–1011; c) H. Liao, Y. Hou, *Chem. Mater.* **2013**, *25*, 457–465; d) H. Liao, J. Zhu, Y. Hou, *Nanoscale* **2014**, *6*, 1049–1055; e) F. Muench, M. Oezaslan, M. Rauber, A. Fuchs, E. Mankel, J. Brötz, P. Strasser, C. Roth, W. Ensinger, *J. Power Sources* **2013**, *222*, 243–252; f) F. Muench, M. Oezaslan, T. Seidl, S. Lauterbach, P. Strasser, H. J. Kleebe, W. Ensinger, *Appl. Phys. A* **2011**, *105*, 847–854; g) F. Muench, M. Oezaslan, I. Svoboda, W. Ensinger, *Mater. Res. Express* **2015**, *2*, 105010.

[3] a) R. Ferrando, J. Jellinek, R. L. Johnston, *Chem. Rev.* **2008**, *108*, 845–910; b) R. Liu, J.-f. Liu, G.-b. Jiang, *Chem. Commun.* **2010**, *46*, 7010–7012; c) S. Tang, S. Vongehr, Y. Wang, J. Cui, X. Wang, X. Meng, *J. Mater. Chem. A* **2014**, *2*, 3648–3660; d) C. Zhu, S. Guo, S. Dong, *Chem. Eur. J.* **2013**, *19*, 1104–1111; e) Z. Zhu, Y. Zhai, C. Zhu, Z. Wang, S. Dong, *Electrochem. Commun.* **2013**, *36*, 22–25.

[4] a) B. Cai, D. Wen, W. Liu, A.-K. Herrmann, A. Benad, A. Eychmüller, *Angew. Chem. Int. Ed.* **2015**, *54*, 13101–13105; *Angew. Chem.* **2015**, *127*, 13293–13297; b) D. Wen, W. Liu, D. Haubold, C. Zhu, M. Oschatz, M. Holzschuh, A. Wolf, F. Simon, S. Kaskel, A. Eychmüller, *ACS Nano* **2016**, *10*, 2559–2567.

[5] a) J. R. Kitchin, J. K. Norskov, M. A. Barteau, J. G. Chen, *J. Chem. Phys.* **2004**, *120*, 10240–10246; b) J. R. Kitchin, J. K. Norskov, M. A. Barteau, J. G. Chen, *Phys. Rev. Lett.* **2004**, *93*, 156801.

[6] D. A. Slanac, W. G. Hardin, K. P. Johnston, K. J. Stevenson, *J. Am. Chem. Soc.* **2012**, *134*, 9812–9819.

[7] B. Hammer, J. K. Norskov, *Adv. Catal.* **2000**, *45*, 71–129.

[8] a) M. Oezaslan, F. Hasché, P. Strasser, *Chem. Mater.* **2011**, *23*, 2159–2165; b) M. Oezaslan, F. Hasché, P. Strasser, *Z. Anorg. Allg. Chem.* **2010**, *636*, 2111–2111.

[9] M. Newville, *J. Synchrotron Radiat.* **2001**, *8*, 322–324.

[10] a) T. J. Schmidt, H. A. Gasteiger, G. D. Stab, P. M. Urban, D. M. Kolb, R. J. Behm, *J. Electrochem. Soc.* **1998**, *145*, 2354–2358; b) T. J. Schmidt, H. A. Gasteiger in *Handbook of Fuel Cells*, Wiley, **2010**.

[11] F. Maillard, E. R. Savinova, U. Stimming, *J. Electroanal. Chem.* **2007**, *599*, 221–232.

[12] M. Hara, U. Linke, T. Wandlowski, *Electrochim. Acta* **2007**, *52*, 5733–5748.

[13] a) F. Hasché, M. Oezaslan, P. Strasser, *Phys. Chem. Chem. Phys.* **2010**, *12*, 15251–15258; b) F. Hasché, M. Oezaslan, P. Strasser, *J. Electrochem. Soc.* **2012**, *159*, B24–B33; c) F. Hasché, M. Oezaslan, P. Strasser, *ChemCatChem* **2011**, *3*, 1805–1813; d) R. L. Borup, J. R. Davey, F. H. Garzon, D. L. Wood, M. A. Inboby, *J. Power Sources* **2006**, *163*, 76–81; e) R. Borup, J. Meyers, B. Pivovar, Y. S. Kim, R. Mukundan, N. Garland, D. Myers, M. Wilson, F. Garzon, D. Wood, P. Zelenay, K. More, K. Stroh, T. Zawodzinski, J. Boncella, J. E. McGrath, M. Inaba, K. Miyatake, M. Hori, K. Ota, Z. Ogumi, S. Miyata, A. Nishikata, Z. Siroma, Y. Uchimoto, K. Yasuda, K.-i. Kimijima, N. Iwashita, *Chem. Rev.* **2007**, *107*, 3904–3951.

[14] a) M. G. Montes de Oca, H. Kumarakuru, D. Cherns, D. J. Fermín, *J. Phys. Chem. C* **2011**, *115*, 10489–10496; b) S. Yun, S. Ted Oyama, *J. Membr. Sci.* **2011**, *375*, 28–45; c) C. Gabrielli, P. P. Grand, A. Lasia, H. Perrot, *J. Electrochem. Soc.* **2004**, *151*, A1937–A1942.

[15] a) H. A. Gasteiger, S. S. Kocha, B. Sompalli, F. T. Wagner, *Appl. Catal. B* **2005**, *56*, 9–35; b) M. Oezaslan, P. Strasser, *J. Power Sources* **2011**, *196*, 5240–5249.

[16] a) B. R. Shrestha, T. Baimpos, S. Raman, M. Valtiner, *ACS Nano* **2014**, *8*, 5979–5987; b) B. R. Shrestha, A. Nishikata, T. Tsuru, *Electrochim. Acta* **2012**, *70*, 42–49; c) B. E. Conway, *Prog. Surf. Sci.* **1995**, *49*, 331–452.

[17] a) A. A. Topalov, I. Katsounaros, M. Auinger, S. Cherevko, J. C. Meier, S. O. Klemm, K. J. J. Mayrhofer, *Angew. Chem. Int. Ed.* **2012**, *51*, 12613–12615; *Angew. Chem.* **2012**, *124*, 12782–12785; b) S. Cherevko, A. R. Zeradjanin, G. P. Keeley, K. J. J. Mayrhofer, *J. Electrochem. Soc.* **2014**, *161*, H822–H830.